




**Effect of spin-orbit coupling in laser-induced ionization of atoms**Yibo Hu,<sup>1</sup> Kunlong Liu <sup>1,\*</sup> Klaus Renziehausen <sup>2</sup> Yidian Tian,<sup>1</sup> Qingbin Zhang,<sup>1</sup> Min Li <sup>1</sup>,  
Yueming Zhou,<sup>1</sup> and Peixiang Lu<sup>1,3,4</sup><sup>1</sup>Wuhan National Laboratory for Optoelectronics and School of Physics,  
Huazhong University of Science and Technology, Wuhan 430074, China<sup>2</sup>Institute of Physical Chemistry and Abbe School of Photonics, Friedrich Schiller University Jena, Lessingstraße 4, 07743 Jena, Germany<sup>3</sup>Hubei Key Laboratory of Optical Information and Pattern Recognition, Wuhan Institute of Technology, Wuhan 430205, China<sup>4</sup>Optics Valley Laboratory, Hubei 430074, China

(Received 9 May 2023; revised 23 July 2023; accepted 25 July 2023; published 8 August 2023)

Based on the expansion of the time-dependent Dirac equation in the second order on the reciprocal of the speed of light, we derive a simplified second-order time-dependent Pauli equation (second-TDPE) for single-active-electron systems, in which the time-dependent spin-orbit interaction is taken into account. A numerical method is presented for calculating the observables for atoms interacting with the electric fields of laser pulses. It is shown that the energy-level splitting between the  $p_{\pm}^{\uparrow}$  and  $p_{\pm}^{\downarrow}$  (as well as the  $p_{\pm}^{\uparrow}$  and  $p_{\pm}^{\downarrow}$ ) orbitals can be reproduced by the spin-orbit coupling (SOC) term of the second-TDPE. By numerically solving the second-TDPE, we demonstrate the SOC effect in single-photon, multiphoton, and tunneling ionization of atomic Kr with valence  $p$  orbitals. In particular, a few counterintuitive strong-field ionization phenomena are discussed and analyzed. The present work provides a convenient way to explore the SOC effect in strong-field interactions.

DOI: [10.1103/PhysRevA.108.023113](https://doi.org/10.1103/PhysRevA.108.023113)**I. INTRODUCTION**

Spin is one of the intrinsic properties of the electron that cannot be described by classical mechanics [1]. The electromagnetic interaction between an electron's spin and its motion inside a potential is called spin-orbit coupling (SOC). In atoms, the SOC plays an important role in the formation of electron energy-level structure, affecting the optical, electrical, and magnetic properties of matter in the interactions with external fields [2–4]. In spite of its importance, the SOC effect was often overlooked in studies in strong-field physics, partially due to the lack of experimental tools to resolve the photoelectron momentum and its spin on an equal footing. It is also challenging to investigate in theory the spin-orbit dynamics in a time-dependent potential during the strong-field ionization.

The SOC is a relativistic effect and, most of the time, is considered too weak to play a role in strong-field interactions for pulse intensities below  $10^{15}$  W/cm<sup>2</sup>. However, the theoretical study by Barth and Smirnova [5] revealed that the SOC, together with the nonadiabatic tunnel ionization, would lead to the spin asymmetry of the photoelectrons. Later on, a few experiments observed the spin-polarized photoelectrons resulting from the nonadiabatic and SOC effects on tunneling [6] and multiphoton ionization [7,8]. The electronic spin and the corresponding SOC have brought the researchers a new degree of freedom to explore the strong-field phenomena.

In previous theoretical calculations [6,7], the SOC effect in strong-field ionization is taken into account by

adjusting the ionization potentials for the atomic models based on the time-dependent Schrödinger equation (TDSE). This approach works well in comparison with the experimental measurements using circularly polarized (CP) laser pulses [6]. Nonetheless, one may be concerned whether such modeling is always fine to be applied [9] because the spin-orbit interaction is a dynamical process in the presence of external laser fields.

To theoretically study the SOC effect, one can apply the time-dependent Dirac equation (TDDE), which incorporates naturally the relativistic effects [10–13]. Yet, numerically solving the TDDE for infrared pulses requires massive computing resources and is time-consuming. Moreover, in TDDE it is not straightforward to exclusively study the SOC effect when other relativistic effects coexist, such as the nondipole effect, the relativistic correction to the kinetic energy, and the generation of positrons. Recently, numerical effort has been made to explore the spin-orbit dynamics in strong-field interactions by adopting the Breit-Pauli Hamiltonian [14]. Here, we turn to a differential equation of the Schrödinger form plus relativistic corrections, which is derived from the expansion of the TDDE up to second order in the reciprocal of the speed of light [15]. As we show in the next section, the equation is similar to the Pauli equation but with second-order terms: A relativistic correction to the kinetic energy, the spin-orbit interaction, and the Darwin term. This differential equation [see Eq. (1)] applied in the present work will be referred to as the second-order time-dependent Pauli equation (second-TDPE).

In this paper, we present the procedure of numerically solving the second-TDPE for the reduced-dimensional atomic models under certain assumptions and approximations. The justification of the assumptions and approximations in our modeling is discussed. Then, we calculate the

\*liukunlong@hust.edu.cn

stationary spin-orbit wave functions for the initial states via the second-TDPE, and their differences from those obtained from the TDSE are shown and discussed. After obtaining the initial wave functions, we investigate the SOC effect on single-photon ionization, multiphoton ionization, and tunneling ionization by calculating the photoelectron momentum distributions (as well as the corresponding kinetic and angular distributions of the photoelectrons) for the  $4p_{+}^{\downarrow}$ ,  $4p_{-}^{\uparrow}$ ,  $4p_{+}^{\uparrow}$ , and  $4p_{-}^{\downarrow}$  orbitals of the single-active-electron atomic model of Kr.

## II. THEORETICAL MODEL

We start with the TDDE approximated up to second order in  $1/c$ , with  $c$  being the speed of light. The corresponding equation, named the second-TDPE in the present work, is given by ( $e = \hbar = m_e = 1$ ) [15]

$$i \frac{\partial \Psi}{\partial t} = \left\{ \frac{1}{2} \hat{\mathbf{P}}^2 - V + \frac{1}{2c} \boldsymbol{\sigma} \mathbf{B} + \frac{1}{8c^2} [\hat{\mathbf{P}}(\boldsymbol{\sigma} \times \mathbf{E}) + (\boldsymbol{\sigma} \times \mathbf{E})\hat{\mathbf{P}}] - \frac{1}{8c^2} \hat{\mathbf{P}}^4 + \frac{1}{8c^2} \nabla \mathbf{E} \right\} \Psi, \quad (1)$$

where the two-spinor  $\Psi = (\psi^{\uparrow}, \psi^{\downarrow})^T$  represents the wave function of a low-energy electron of spin  $1/2$ ,  $\hat{\mathbf{P}} = \hat{\mathbf{p}} + \mathbf{A}$  is the kinematic momentum operator with  $\mathbf{A}$  being the vector potential of the laser field, and  $\boldsymbol{\sigma} = (\sigma^1, \sigma^2, \sigma^3)$  is the vector formed by the three Pauli matrices.

On the right-hand side of Eq. (1), the first term indicates the kinetic energy of the electron in an electromagnetic field, the second term is its potential energy in the electrostatic potential  $V$ , and the rest are the terms of relativistic corrections. In details, the third term is the first-order correction that describes the Zeeman splitting in a magnetic field  $\mathbf{B} = \nabla \times \mathbf{A}$ . The fourth term, which will be abbreviated by  $\hat{H}_{so}$ , describes spin-orbit interactions in the electric field defined as  $\mathbf{E} = -\nabla V - \partial \mathbf{A} / \partial t$ . In particular, for static fields with a centrally symmetric potential  $V(\mathbf{r}) = V(r)$ , we have  $\mathbf{A} = \mathbf{B} = \mathbf{0}$  and  $\mathbf{E} = -(\mathbf{r}/r)(\partial/\partial r)V(r)$ . Then, one finds that  $\hat{H}_{so}$  is proportional to an operator  $\hat{\mathbf{S}} \cdot \hat{\mathbf{L}}$ , where  $\hat{\mathbf{S}} = \boldsymbol{\sigma}/2$  is the so-called spin operator and  $\hat{\mathbf{L}} = \mathbf{r} \times \hat{\mathbf{p}}$  is the angular-momentum operator. Therefore,  $\hat{H}_{so}$  is called the spin-orbit interaction term. The term before the last one is related to a relativistic correction of the kinetic energy, and the last one is the so-called Darwin term, a relativistic correction that is related to the charge density  $\rho = \nabla \mathbf{E} / (4\pi)$  in the system.

In the present work, our aim is to study the spin-orbit coupling effect in strong-field interactions and facilitate the numerical calculations. Thus, we establish our model by applying the following approximations and assumptions. First of all, we apply the single-active-electron (SAE) approximation, which is commonly used in strong-field studies. Second, we neglect the nondipole effect, the Zeeman term, the relativistic correction to the kinetic energy, and the Darwin term. The justifications of these approximations can be found in the Appendix. Then, the second-TDPE is simplified as

$$i \frac{\partial \Psi}{\partial t} = \left[ \frac{1}{2} \hat{\mathbf{P}}^2 - V + \frac{1}{4c^2} \boldsymbol{\sigma} (\mathbf{E} \times \hat{\mathbf{P}}) \right] \Psi. \quad (2)$$

By substituting  $\Psi$ ,  $\boldsymbol{\sigma}$ , and  $\mathbf{E}$  in Eq. (2) with their specific forms, we obtain the coupled TDPEs for the wave functions of the spin-up and spin-down electrons as

$$i \frac{\partial \psi^{\uparrow}}{\partial t} = \left[ \frac{1}{2} \hat{\mathbf{P}}^2 - V + \frac{1}{4c^2} (E_x \hat{\Pi}_y - E_y \hat{\Pi}_x) \right] \psi^{\uparrow} + \frac{1}{4c^2} [(E_y + iE_x) \hat{\Pi}_z - E_z (\hat{\Pi}_y + i\hat{\Pi}_x)] \psi^{\downarrow}, \quad (3)$$

$$i \frac{\partial \psi^{\downarrow}}{\partial t} = \left[ \frac{1}{2} \hat{\mathbf{P}}^2 - V - \frac{1}{4c^2} (E_x \hat{\Pi}_y - E_y \hat{\Pi}_x) \right] \psi^{\downarrow} + \frac{1}{4c^2} [(E_y - iE_x) \hat{\Pi}_z - E_z (\hat{\Pi}_y - i\hat{\Pi}_x)] \psi^{\uparrow}. \quad (4)$$

The coupling between  $\psi^{\uparrow}$  and  $\psi^{\downarrow}$  seen in Eqs. (3) and (4) indicates the possibility of the spin-flip process. Considering the nonrelativistic pulse intensities used in the present study and that the spin-flip probability is generally small with respect to the total ionization rate [11], we further omit the spin-flip process of the electron in our calculation. By doing so, we finally reach the aimed form of the second-TDPE, which is written as

$$i \frac{\partial \psi^{\uparrow, \downarrow}}{\partial t} = \left[ \frac{1}{2} \hat{\mathbf{P}}^2 - V \pm \frac{1}{4c^2} (E_x \hat{\Pi}_y - E_y \hat{\Pi}_x) \right] \psi^{\uparrow, \downarrow}. \quad (5)$$

Note that the third term on the right-hand side of Eq. (5) is Hermitian for  $(\nabla \times \mathbf{E})_z = 0$ , which is indeed the case in our model. In addition, the sign “ $\pm$ ” of this term distinguishes the SOC effect on the spin-up and spin-down electrons.

Next, we apply the simplified second-TDPE to the two-dimensional models for the noble gas atoms, assuming that the laser pulse is polarized in the  $x$ - $y$  plane. The soft-core potential is given by

$$V(r) = \frac{1 + (Z - 1)e^{-br^2}}{\sqrt{r^2 + a}}, \quad (6)$$

with  $Z$  being the atomic charge number and  $a$  and  $b$  the parameters to reproduce the ionization potential of the considered atom. The vector potential  $\mathbf{A}$  within the dipole approximation is given by

$$\mathbf{A}(t) = \frac{E_0}{\omega} \sin^4 \left( \frac{\omega t}{2N} \right) [-\epsilon \sin(\omega t) \mathbf{e}_x + \cos(\omega t) \mathbf{e}_y] \quad (7)$$

for  $0 \leq t \leq NT$  and  $\mathbf{A}(t) = \mathbf{0}$  outside this interval. Here,  $E_0$ ,  $\omega$ ,  $T = 2\pi/\omega$ , and  $N$  indicate the electric-field amplitude, the laser frequency, the optical period, and the number of the optical cycles of the full pulse, respectively, and  $\epsilon \in [-1, 1]$  determines the ellipticity of the laser pulse in our simulations.

## III. NUMERICAL METHOD

For simplification of the discussion of numerically solving Eq. (5), we rewrite the equation as

$$i \frac{\partial \psi}{\partial t} = \left[ \frac{1}{2} \hat{\mathbf{P}}^2 - V + \frac{S}{4c^2} (E_x \hat{\Pi}_y - E_y \hat{\Pi}_x) \right] \psi. \quad (8)$$

By setting the parameter  $S = \pm 1$  and  $S = 0$  in Eq. (8), we can reach the equations for the spin-up, spin-down, and spinless (equivalent to TDSE) cases, respectively. Then, Eq. (8) is numerically solved by using the split-operator method [16].

The approximate evolution of the wave function is described by

$$\begin{aligned} \psi(t + \delta t) \approx & \exp \left\{ -i \frac{\delta t}{2} \left[ \frac{\mathcal{S}}{4c^2} (E_x A_y - E_y A_x) - V \right] \right\} \\ & \times \exp \left[ -i \frac{\delta t}{2} \frac{\mathcal{S}}{4c^2} (E_x \hat{p}_y - E_y \hat{p}_x) \right] \\ & \times \exp \left[ -i \delta t \frac{1}{2} (\hat{\mathbf{p}} + \mathbf{A})^2 \right] \\ & \times \exp \left[ -i \frac{\delta t}{2} \frac{\mathcal{S}}{4c^2} (E_x \hat{p}_y - E_y \hat{p}_x) \right] \\ & \times \exp \left\{ -i \frac{\delta t}{2} \left[ \frac{\mathcal{S}}{4c^2} (E_x A_y - E_y A_x) - V \right] \right\} \psi(t). \end{aligned} \quad (9)$$

In Eq. (9), the first and final exponential operations on the wave function can be calculated directly in the coordinate space, while the third one can be calculated in the momentum space via Fourier transformation of the wave function. In the second and fourth operations, the electric field  $\mathbf{E} = -\nabla V - \partial \mathbf{A} / \partial t = (E_x, E_y)$  that depends on the coordinate is multiplied by the momentum operator, indicating that they can no longer be calculated directly in either coordinate or momentum space. Thus, we turn to the equivalent evaluation of the second (fourth) operation by numerically solving the following partial equation:

$$\begin{aligned} i \frac{\partial \psi}{\partial t} &= \frac{\mathcal{S}}{8c^2} (E_x \hat{p}_y - E_y \hat{p}_x) \psi \\ &= i \frac{\mathcal{S}}{8c^2} \left( -E_x \frac{\partial}{\partial y} + E_y \frac{\partial}{\partial x} \right) \psi \end{aligned} \quad (10)$$

for one time step. To this end, the alternating direction implicit method [17] is applied. In details, we split the propagation for a time step of  $\delta t$  into two steps of  $\delta t/2$  as following

$$i \frac{\psi_{k,j}^{n+\frac{1}{2}} - \psi_{k,j}^n}{\delta t/2} = \frac{i\mathcal{S}}{8c^2} \left( E_y \frac{\partial}{\partial x} \psi_{k,j}^n - E_x \frac{\partial}{\partial y} \psi_{k,j}^{n+\frac{1}{2}} \right), \quad (11)$$

$$i \frac{\psi_{k,j}^{n+1} - \psi_{k,j}^{n+\frac{1}{2}}}{\delta t/2} = \frac{i\mathcal{S}}{8c^2} \left( E_y \frac{\partial}{\partial x} \psi_{k,j}^{n+\frac{1}{2}} - E_x \frac{\partial}{\partial y} \psi_{k,j}^{n+1} \right), \quad (12)$$

where  $n$  and  $(k, j)$  are the indexes for the discrete time and space, respectively, and the values of  $E_x$  and  $E_y$  are adopted at the time indexed by  $(n + \frac{1}{2})$  and in the space indexed by  $(k, j)$ . By doing so, we break the two-dimensional time-propagation problem into two one-dimensional ones, which can now be solved using the finite difference scheme, similarly to the Crank-Nicolson method [18]. That is, we can obtain  $\psi^{n+\frac{1}{2}}$  by solving Eq. (11) for the one-dimensional wave function  $\psi(x_k, y)$  at each  $x_k$  in parallel and then  $\psi^{n+1}$  from Eq. (12) in the same way but for  $\psi(x, y_j)$ . So far, the propagation of one time step of the wave function given in Eq. (10) and thus that in Eq. (9) can be accomplished.

To avoid the nonphysical reflection of the wave function from the boundary of the calculation box, the wave function is smoothly split into the inner and outgoing parts in real-time propagation with an absorption function [19]. We assume that the Coulomb potential and the Coulomb field are negligible

in the regime far from the core. Thus, the inner wave function is propagated under full Hamiltonian, while the outgoing one representing the ionizing part is analytically propagated under the Volkov Hamiltonian

$$H_V = \frac{1}{2} \hat{\mathbf{\Pi}}^2 + \frac{\mathcal{S}}{4c^2} \left( -\frac{\partial A_x}{\partial t} \hat{\Pi}_y + \frac{\partial A_y}{\partial t} \hat{\Pi}_x \right), \quad (13)$$

in which the Coulomb potential  $V$  and the corresponding static electric field is neglected. The analytical ‘‘Volkov phase’’ is given by

$$\begin{aligned} S(t_1, t_2) &= \frac{1}{2} \int_{t_1}^{t_2} \mathbf{\Pi}^2(\tau) d\tau \\ &+ \frac{\mathcal{S}}{4c^2} \int_{t_1}^{t_2} \left[ -\frac{\partial A_x(\tau)}{\partial t} \Pi_y + \frac{\partial A_y(\tau)}{\partial t} \Pi_x \right] d\tau \\ &= S_0(t_1, t_2) + S_{so}(t_1, t_2), \end{aligned} \quad (14)$$

where  $S_0(t_1, t_2)$  is the same as the Volkov phase for Coulomb-free TDSE [20] and  $S_{so}(t_1, t_2)$  is an extra phase coming from the spin-orbit interaction for the freed electron in the external field.

To calculate the photoelectron momentum distribution (PMD), the outgoing wave-function split at  $\tau$  is first transformed from the coordinate space to the momentum space and then is propagated from time  $\tau$  until  $t_{\text{end}}$ , i.e., the end of the simulation, under the Volkov Hamiltonian given by Eq. (13). By superposing the outgoing wave functions in the momentum space at  $t_{\text{end}}$ , we can eventually obtain the PMD for the interaction [21].

In our numerical simulations, there are  $3000 \times 3000$  grid points of the box and the spacing steps are  $\Delta x = \Delta y = 0.1$  a.u. The time step for the propagation of the wave function is chosen as  $\delta t = 0.01$  a.u. We recall that one can conveniently switch the calculations between the spin-up, spin-down, and spinless cases by setting  $\mathcal{S} = \pm 1$  and  $\mathcal{S} = 0$ , respectively.

## IV. SIMULATION RESULTS

### A. Initial states

To begin with, we illustrate the electron wave functions of the initial states calculated via the second-TDPE and discuss the differences from those calculated via the TDSE. Since the outermost electron of the noble gas atoms except helium is in the  $p$  orbital, and the ionization of  $m = 0$  state is strongly suppressed [5], we only consider the  $p_{\pm}$  orbitals with  $m = \pm 1$  in this paper.

Due to the SOC effect, the removal of the  $p$ -orbital electron of noble gas atoms would lead to the ion populated in the state of  $^2P_{3/2}$  or  $^2P_{1/2}$  [5], providing two ionization channels with different ionization potentials. In the present study, we define  $I_p^{1/2}$  and  $I_p^{3/2}$  as the ionization potentials for the single-active-electron orbitals corresponding to the lower and higher energy levels, respectively. Previous works based on the TDSE reproduce the spin-orbit energy splitting by adjusting the parameters of the Coulomb potentials [6,7]. In contrast, in the present calculations, the energy splitting arises from the spin-orbit coupling term in the second-TDPE for  $p_{\pm}$  orbitals with  $\mathcal{S} = \pm 1$ .

According to Eq. (8), the field-free electronic Hamiltonian of the second-TDPE is given by

$$H_0 = \frac{1}{2}\hat{\mathbf{p}}^2 - V - \frac{\mathcal{S}}{4c^2} \left( \frac{\partial V}{\partial x} \hat{p}_y - \frac{\partial V}{\partial y} \hat{p}_x \right). \quad (15)$$

Since the specific form of  $V$  is already known in Eq. (6), its partial derivative can be derived as

$$\frac{\partial V}{\partial x} = -\hat{Q}(r)\hat{x}, \quad \frac{\partial V}{\partial y} = -\hat{Q}(r)\hat{y}, \quad (16)$$

where

$$\hat{Q}(r) = \frac{1 + [(Z-1) + 2b(Z-1)(r^2 + a)]e^{-br^2}}{(r^2 + a)^{3/2}} \quad (17)$$

is an operator related to the distance between the electron and the core. Accordingly, we can obtain

$$\begin{aligned} H_0 &= \frac{1}{2}\hat{\mathbf{p}}^2 - V + \frac{\hat{Q}(r)}{4c^2} \mathcal{S}(\hat{x}\hat{p}_y - \hat{y}\hat{p}_x) = \frac{1}{2}\hat{\mathbf{p}}^2 - V + \frac{\hat{Q}(r)}{4c^2} \mathcal{S}\hat{L}_z \\ &= \frac{1}{2}\hat{\mathbf{p}}^2 - V + H_{so}^0, \end{aligned} \quad (18)$$

where  $\hat{L}_z = \hat{x}\hat{p}_y - \hat{y}\hat{p}_x$  is the  $z$  component of the angular momentum operator  $\hat{\mathbf{L}}$ . For the  $p_{\pm}$  orbitals considered in this paper, we have

$$\hat{L}_z |p_{\pm}\rangle = \pm |p_{\pm}\rangle. \quad (19)$$

Therefore, for an atomic orbital with given helicity and electronic spin orientation, the extra energy  $\mathcal{E}_{so} = \langle H_{so}^0 \rangle$  due to the SOC effect can be calculated. Specifically, we have

$$\mathcal{E}_{so} \begin{cases} = \frac{\langle \hat{Q}(r) \rangle}{4c^2}, & \text{for } p_+^{\uparrow} \text{ and } p_-^{\downarrow} \\ = -\frac{\langle \hat{Q}(r) \rangle}{4c^2}, & \text{for } p_+^{\downarrow} \text{ and } p_-^{\uparrow} \end{cases}, \quad (20)$$

where  $p_{\pm}^{\uparrow}$  and  $p_{\pm}^{\downarrow}$  denote the atomic orbitals with  $m = \pm 1$  and  $\mathcal{S} = \pm 1$ . Hence, the initial energies of these four orbitals will split into two energy levels.

To reproduce the correct energy splitting, further numerical processing is necessary. In detail, we first adjust the soft-core parameters  $a$  and  $b$  so that the binding energy of the spinless  $p$  electron satisfies

$$\mathcal{E}_o = \left\langle \frac{1}{2}\hat{\mathbf{p}}^2 - V \right\rangle = -\frac{I_p^{1/2} + I_p^{3/2}}{2}. \quad (21)$$

Then, a SOC parameter  $d$  is introduced to the Coulomb electric field as

$$\mathbf{E} = -d^2 \nabla V - \partial \mathbf{A} / \partial t, \quad (22)$$

so that we can adjust the magnitude of the energy splitting to satisfy

$$|\mathcal{E}_{so}| = |\langle H_{so}^0 \rangle| = d^2 \frac{\langle \hat{Q}(r) \rangle}{4c^2} = \frac{I_p^{1/2} - I_p^{3/2}}{2}. \quad (23)$$

By doing so, reproduce two ionization potentials for the  $p_m^{\uparrow, \downarrow}$  of the given atomic model. Specifically, we have

$$I_p(p_+^{\uparrow}) = I_p(p_-^{\downarrow}) = -(\mathcal{E}_o + |\mathcal{E}_{so}|) = I_p^{3/2}, \quad (24)$$

$$I_p(p_+^{\downarrow}) = I_p(p_-^{\uparrow}) = -(\mathcal{E}_o - |\mathcal{E}_{so}|) = I_p^{1/2}, \quad (25)$$

TABLE I. The parameters for the Coulomb potentials and the SOC effect, as well as the corresponding binding energies, for three different types of atoms.

	$Z$	$a$	$b$	$d$	$-I_p^{3/2}$	$-I_p^{1/2}$	Orbital
Ne	10	2.878	1.000	5.771	-0.7924	-0.7959	$2p$
Kr	36	3.962	0.456	16.842	-0.5150	-0.5390	$4p$
Xe	54	14.950	0.200	38.482	-0.4457	-0.4939	$5p$

where  $-I_p^{3/2} > -I_p^{1/2}$ . The parameters for the Coulomb potential and the SOC effect for three types of atoms (Ne, Kr, and Xe) have been adjusted in our calculations. Their values and the corresponding binding energies are given in Table I.

To show, as an example, the differences between the bound states for  $p$  orbitals obtained from the TDSE and the second-TDPE, we calculate the electronic wave functions of the second and the third bound states for the model atom of Ne. The calculation is carried out with the imaginary-time propagation method [22]. In the TDSE simulations, the second and the third bound states are degenerate and correspond to the  $2p$  orbitals for Ne. The imaginary-time propagation of the TDSE leads to the real-valued stationary wave functions, and the electronic density distributions are shown in Figs. 1(a) and 1(b). Both orbitals exhibit the oriented two-lobe structures. As indicated by the black dashed lines in Figs. 1(a) and 1(b), the orientations of two distributions are always perpendicular to each other, since these two states are orthogonal. In contrast, the second and the third bound states calculated via the second-TDPE differ from those of the TDSE. Due to the SOC effect, the binding energies of the  $2p$  electrons are no longer degenerate. For the spin-up electron, for example, the imaginary-time propagation of the second-TDPE converges to the stationary wave function of the  $2p_-^{\uparrow}$  orbital in the lower energy level (with ionization potential  $I_p^{1/2}$ ) and then to the one for the  $2p_+^{\uparrow}$  orbital in the relatively higher energy level (with ionization potential  $I_p^{3/2}$ ). Note that the SOC term in Eq. (18) guarantees that the values of the stationary wave function could be complex numbers in the imaginary-time propagation. Figures 1(c) and 1(d) and Figs. 1(e) and 1(f) illustrate the probability density and phase distributions of the  $2p$  orbitals for spin-up electrons, respectively. It shows that the density distributions in the second-TDPE appear as a ring structure. From the rotational phase distributions, one can identify the orbitals as the  $2p_-^{\uparrow}$  [Fig. 1(c)] and  $2p_+^{\uparrow}$  [Fig. 1(d)] orbitals, respectively.

By adopting the parameters given in Table I, one can also obtain the stationary wave functions of  $4p_m^{\uparrow}$  and  $4p_m^{\downarrow}$  orbitals for Kr and  $5p_m^{\uparrow}$  and  $5p_m^{\downarrow}$  orbitals for Xe, based on the imaginary-time propagation of the second-TDPE. The electronic density distributions of the  $4p_+^{\uparrow}$  orbital for Kr and that of the  $5p_+^{\uparrow}$  orbital for Xe are shown in Figs. 2(a) and 2(b), respectively.

## B. Single-photon ionization

By numerically solving the second-TDPE, we demonstrate the effect of SOC on single-photon ionization (SPI) in this section. We calculated the photoelectron momentum

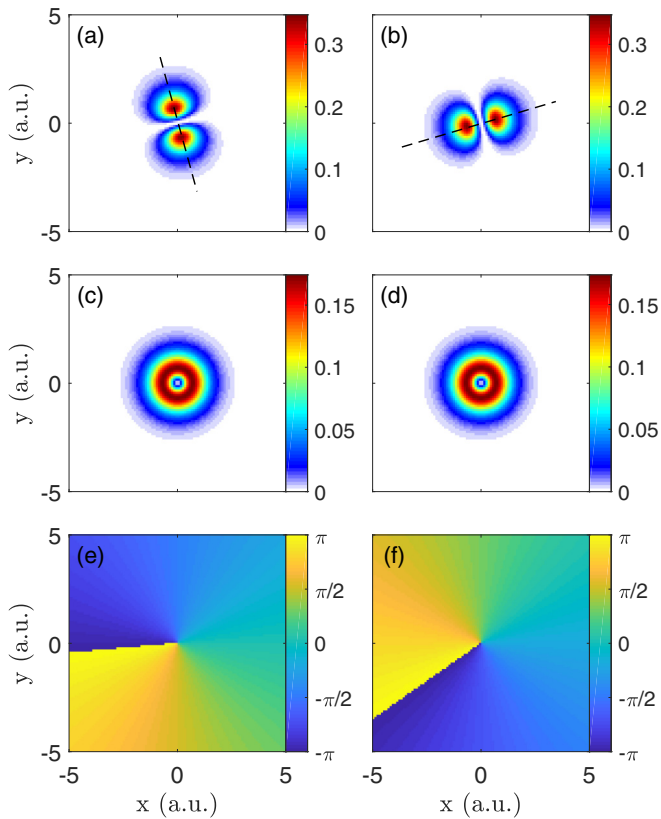


FIG. 1. (a)–(d) The electronic probability density (e), (f) and phase distributions of the second (left column) and the third (right column) bound orbitals of Ne atom calculated via the imaginary-time propagation method. Panels (a) and (b) are the results obtained from the TDSE, while panels (c)–(f) are the results obtained from the second-TDPE with  $\epsilon=1$ . The black dashed lines in panels (a) and (b) indicate the orientation of the distributions.

distributions of the SPI by a linearly polarized XUV pulse. Figures 3(a)–3(d) illustrate the PMDs for four initial  $4p_m^\uparrow$  and  $4p_m^\downarrow$  orbitals of Kr driven by a  $y$ -polarized laser pulse with  $\omega = 1.8$  a.u. One can observe the tilted two-lobe structures of the PMDs. The two-lobe structures can be explained by the interference between the  $s$  and  $d$  waves of the final electronic states with different magnetic quantum numbers [23], while their tilted direction depends on the initial orbital angular momentum [24].

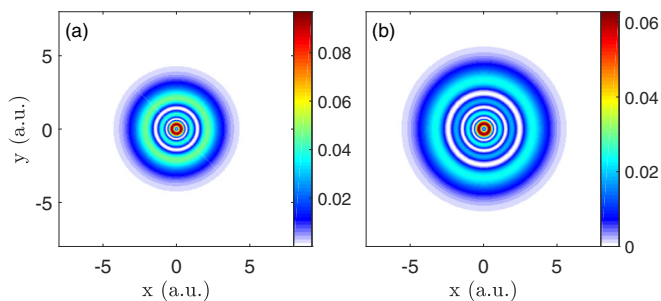


FIG. 2. The electronic probability density distributions of the (a)  $4p_+^\uparrow$  orbital for Kr and the (b)  $5p_+^\uparrow$  orbital for Xe.

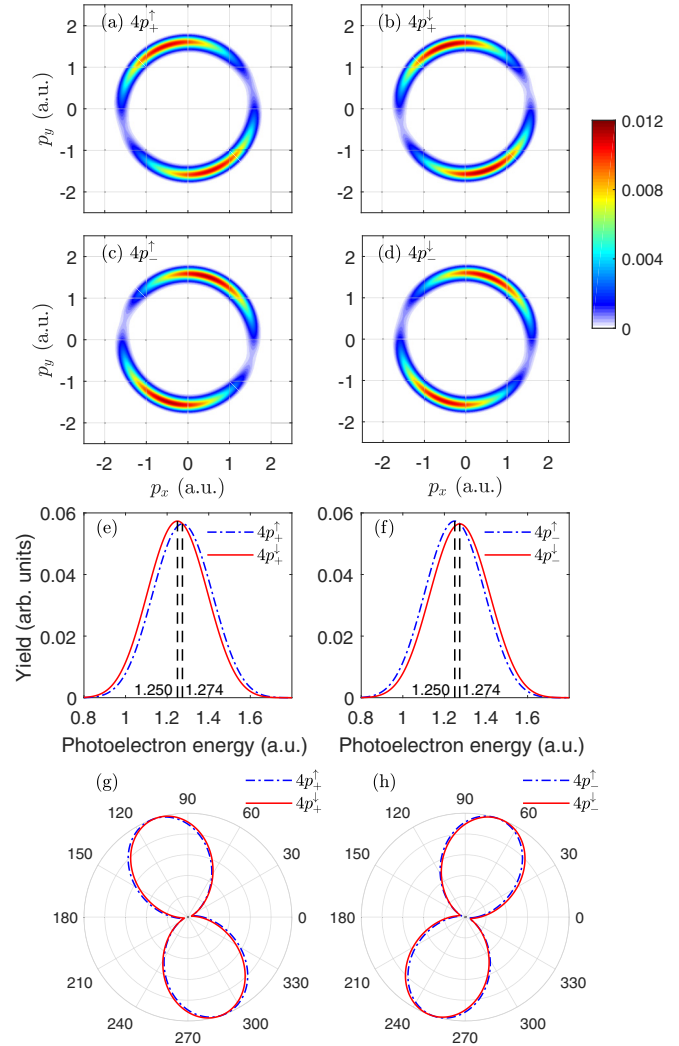


FIG. 3. The PMDs for the (a)  $4p_+^\uparrow$ , (b)  $4p_+^\downarrow$ , (c)  $4p_-^\uparrow$ , and (d)  $4p_-^\downarrow$  atomic orbitals of Kr in a  $y$ -polarized XUV laser pulse with  $\omega = 1.8$  a.u.,  $E_0 = 0.1$  a.u. (corresponding to the intensity  $I = 3.5 \times 10^{14}$  W/cm<sup>2</sup>) and  $N = 10$ . The corresponding PEDs and PADs are shown in panels (e), (f) and (g), (h), respectively. The vertical dashed lines depicted in panels (e) and (f) indicate the location of the peaks of the corresponding PEDs.

To demonstrate the effect of the electron spin on the PMDs more clearly, we also calculated the photoelectron energy distributions (PEDs) and photoelectron angular distributions (PADs) from the corresponding PMDs. The results are shown in Figs. 3(e)–3(h), respectively. From the PEDs, on one hand, we can see an energy shift between the  $4p_+^\uparrow$  and  $4p_+^\downarrow$  orbitals [Fig. 3(e)], as well as that between the  $4p_-^\downarrow$  and  $4p_-^\uparrow$  orbitals [Fig. 3(f)]. As indicated by the vertical dashed lines in Figs. 3(e) and 3(f), the energy shift between the maxima of two PEDs is about 0.024 a.u., approximately equal to the spin-orbit energy splitting between the corresponding orbitals. From the PADs [Figs. 3(g) and 3(h)], on the other hand, we can see that the values of the tilting angle for opposite spins are slightly different. In particular, the PADs of spin-up and spin-down electrons are relatively rotated counterclockwise and clockwise, respectively, for both  $p_+$  and  $p_-$  orbitals.

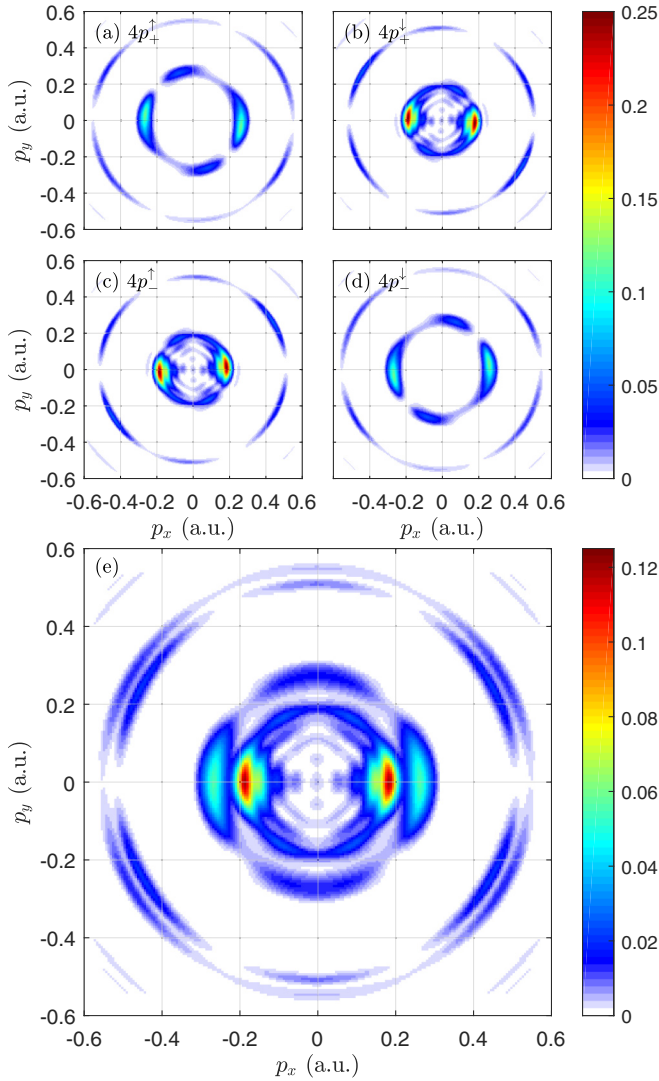


FIG. 4. The PMDs for the (a)  $4p_+^\uparrow$ , (b)  $4p_+^\downarrow$ , (c)  $4p_-^\uparrow$ , and (d)  $4p_-^\downarrow$  atomic orbitals of Kr ionized by a y-polarized laser pulse with the laser wavelength of 400 nm (corresponding to the frequency  $\omega = 0.114$  a.u.),  $I = 3.2 \times 10^{13}$  W/cm<sup>2</sup>, and  $N = 24$ . The average distribution of the four PMDs for the  $p_m^\uparrow$  and  $p_m^\downarrow$  orbitals is shown in panel (e).

Although the SOC effect on the PMDs in SPI seems rather small, as the Hamiltonian  $\hat{H}_{so}$  is almost negligible for low-velocity photoelectrons removed by a single photon, our numerical results still show that in addition to the kinetic energy shift, the SOC also deflects the momentum direction of the photoelectron.

### C. Multiphoton ionization

In this section, we show the simulation results for the multiphoton ionization of atomic Kr driven by a 400-nm, multicycle linearly polarized pulse. The PMDs for the  $4p_m^\uparrow$  and  $4p_m^\downarrow$  orbitals are shown in Figs. 4(a)–4(d), respectively. The electric field is polarized along the y axis and the pulse intensity is  $3.2 \times 10^{13}$  W/cm<sup>2</sup>. One can see the pronounced difference between the PMDs for the  $4p_+^\uparrow$  and  $4p_+^\downarrow$  orbitals, as well as those for the  $4p_-^\uparrow$  and  $4p_-^\downarrow$  orbitals. That is, for the initial or-

bitals carrying the same nonzero angular momentum, the momentum distributions of the spin-up and spin-down photoelectrons differ from each other. It indicates that the SOC has significant impact on the photoelectrons in multiphoton ionization driven by the linearly polarized pulses. Then, we calculate the average of the four PMDs for the  $4p_m^\uparrow$  and  $4p_m^\downarrow$  orbitals and show the result in Fig. 4(e). The ring structures, originating from the absorption of multiple photons, can be clearly seen in the averaged PMD. In particular, the ring at the momentum of around 0.19 a.u. (0.26 a.u.) corresponds to the five-photon ionization of the  $4p_+^\downarrow$  and  $4p_-^\uparrow$  ( $4p_+^\uparrow$  and  $4p_-^\downarrow$ ) orbitals. The splitting rings for the six-photon ionization of Kr are also observable from the PMDs. More importantly, we notice that, for the five-photon ionization channel, the yield for the photoelectrons emitting in the direction perpendicular to the laser polarization is larger than that along the laser polarization. Note that this anomalous phenomenon was reported in previous experimental studies under the similar laser conditions [9,25].

This counterintuitive angular distribution of the photoelectrons can be interpreted as the ionization path interference modified by the SOC effect. When the atom is ionized via absorbing photons in a linearly polarized laser pulse, the PMD is formed by the interference between different ionization paths. In the case of five-photon ionization of a  $4p_+$  initial state, for example, the allowed quantum numbers are  $l = 0, 2, 4$ , and 6 and  $m = -4, -2, 0, 2, 4$ , and 6 within the electric-dipole approximation. Then, the dependence of the final-state wave function in the momentum space on the azimuthal angle  $\phi$  is given by [26]

$$\psi(\mathbf{p}) = \sum_{l,m} a_{lm}(p) e^{im\phi + i\delta(S,l,m)}, \quad (26)$$

with  $a_{lm}$  relating to the complex amplitudes of the contributing partial waves. Note that the additional phase term  $\delta(S, l, m)$  in Eq. (26) represents the phase introduced by the SOC [see Eq. (14)], which depends on the spin orientation as well as the quantum numbers  $l$  and  $m$ . Therefore, the interference of the possible ionization paths affected by SOC eventually modifies the angular distribution of photoelectrons. Then, certain SOC phases contributing to the final state could eventually lead to the perpendicular emission of the photoelectrons as observed.

Next, we investigate the dependence of the photoelectron energy spectrum on the pulse intensity ranging from  $2.4 \times 10^{13}$  to  $6.4 \times 10^{13}$  W/cm<sup>2</sup>. The results averaged over the  $4p_m^\uparrow$  and  $4p_m^\downarrow$  orbitals are illustrated in Fig. 5. The spectrum at each intensity is normalized to the peak value. In general, the photoelectron energy decreases linearly with the increasing intensity. This is consistent with the feature of above-threshold ionization where the photoelectron kinetic energy is shifted by the ponderomotive potential [27]. For a given  $n$ -photon ionization channel, we also find that the relative yields of the two splitting spectrum peaks flip when the pulse intensity passes about  $3.6 \times 10^{13}$  W/cm<sup>2</sup>. In particular, at the intensities below  $3.6 \times 10^{13}$  W/cm<sup>2</sup>, the ionization yield corresponding to the lower bound energy level ( $-I_p^{1/2}$ ) is higher, as indicated by the solid arrows in Fig. 5, whereas normally the ionization from the higher level ( $-I_p^{3/2}$ ) is expected to be easier, like those indicated by the dashed arrows. This phenomenon was observed in the previous experimental

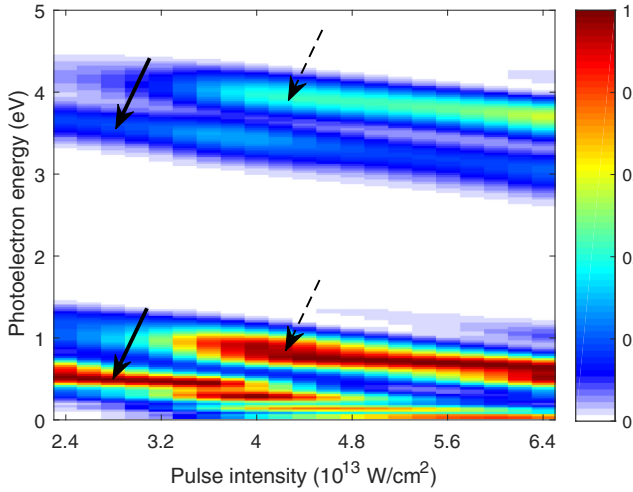


FIG. 5. The photoelectron energy spectra as a function of the pulse intensity in the linearly polarized pulse. The other laser parameters are the same as those in Fig. 4. The solid and dashed arrows point at the ionization peaks are associated with the atomic orbitals in the energy levels of  $-I_p^{1/2}$  and  $-I_p^{3/2}$ , respectively.

studies on multiphoton ionization of Kr in ultraviolet laser fields [9,25].

This intensity-dependent trend is likely due to the resonant excitation during the interaction. In our simulations, we find that the binding-energy difference between the  $4p$  ( $I_p^{3/2} = 0.5150$  a.u. and  $I_p^{1/2} = 0.5390$  a.u.) and  $5p$  ( $I_p^{3/2} = 0.0861$  a.u. and  $I_p^{1/2} = 0.0868$  a.u.) orbitals is about four photon energies (0.1139 a.u.). It indicates that, during the interaction there could be resonant excitation to the  $5p$  orbitals, which would significantly modify the ionization yield. Then, we calculate the excited populations in the  $5p_m^\uparrow$  and  $5p_m^\downarrow$  orbitals at the end of the interactions. The results as a function of the pulse intensity for four initial orbitals are shown in Figs. 6(a)–6(d), respectively. We can indeed find certain populations remaining in the  $5p_m^\uparrow$  and  $5p_m^\downarrow$  orbitals, indicating the resonant excitation during the interactions. We also check that the remaining population of other excited states are less than  $10^{-6}$ , three orders lower with respect to those of the  $5p_m^\uparrow$  and  $5p_m^\downarrow$  orbitals. From Fig. 6, one can see that the remaining populations in  $5p_m^\uparrow$  and  $5p_m^\downarrow$  orbitals increase with the intensity for the initial  $4p_{+}^\uparrow$  and  $4p_{-}^\downarrow$  orbitals [Figs. 6(a) and 6(d)], which contribute to the splitting peaks at relatively higher energy of the spectra (indicated by dashed arrows in Fig. 5). In contrast, the excited population hardly changes for the  $4p_{+}^\downarrow$  and  $4p_{-}^\uparrow$  orbitals [Figs. 6(b) and 6(c)], which contribute to the splitting peaks at relatively lower energy of the spectra (indicated by solid arrows in Fig. 5). Then, we sum up the remaining excited population associated with the higher and lower splitting spectrum peaks, respectively, and show the results in Fig. 7. Interestingly, two curves cross near the intensity of  $4 \times 10^{13}$  W/cm<sup>2</sup>. Note that higher resonant excitation would normally enhance the ionization yield. This explains, to some extent, why the ionization yields for the splitting peaks flip as the pulse intensity changes from  $2.4 \times 10^{13}$  W/cm<sup>2</sup> to  $6.4 \times 10^{13}$  W/cm<sup>2</sup>.

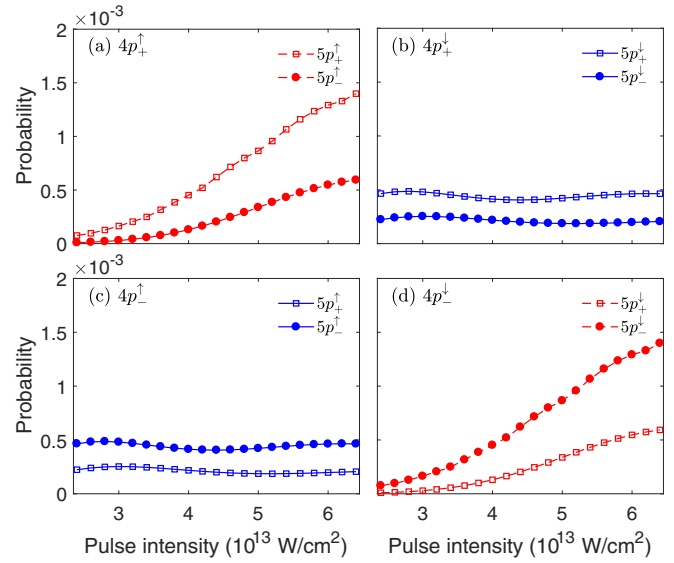


FIG. 6. The excited populations in  $5p_m^\uparrow$  and  $5p_m^\downarrow$  orbitals at the end of the interactions as a function of the pulse intensity for the initial (a)  $4p_{+}^\uparrow$ , (b)  $4p_{+}^\downarrow$ , (c)  $4p_{-}^\uparrow$ , and (d)  $4p_{-}^\downarrow$  orbitals.

#### D. Tunneling ionization

Laser-induced tunneling ionization of atoms and molecules is one of the most fundamental strong-field processes in attosecond science [28–32]. In this section, we investigate the SOC effect on tunneling ionization driven by a circularly polarized laser pulse. Figures 8(a)–8(d) demonstrate the PMDs for the  $4p_m^\uparrow$  and  $4p_m^\downarrow$  orbitals of Kr in an 800-nm, three-cycle right circularly polarized (RCP) pulse, the negative vector potential of which is depicted by the solid curves. In general, the PMDs exhibit the typical patterns of attoclock angular streaking [33–37]. The photoelectron momentum drifts for

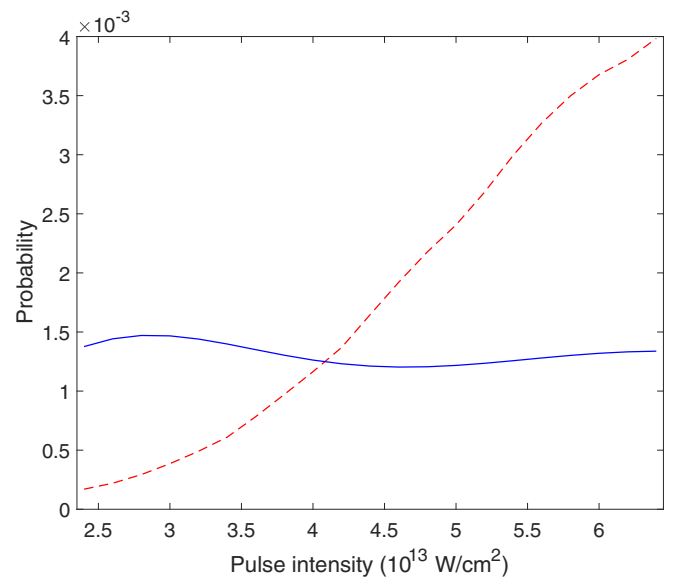


FIG. 7. The remaining excited population associated with the higher (dashed curve) and lower (solid curve) splitting peaks of the spectra shown in Fig. 5.

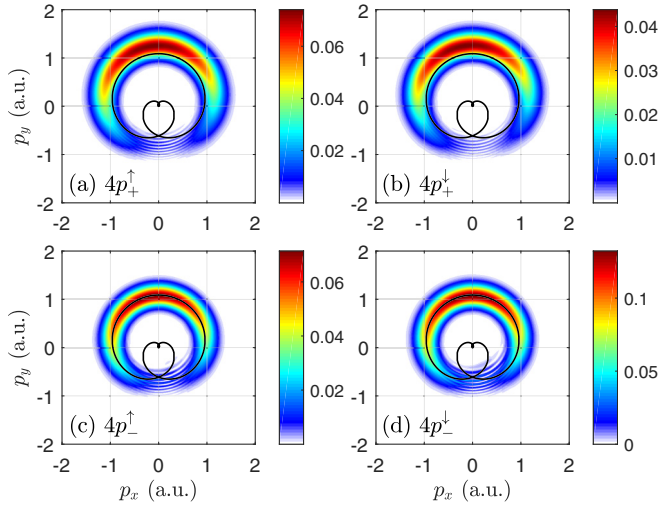


FIG. 8. The PMDs for the (a)  $4p_+^{\uparrow}$ , (b)  $4p_+^{\downarrow}$ , (c)  $4p_-^{\uparrow}$  and (d)  $4p_-^{\downarrow}$  atomic orbitals of Kr in a three-cycle RCP laser pulse with the wavelength of 800 nm (corresponding to the frequency  $\omega = 0.057$  a.u.) and the intensity of  $I = 1.35 \times 10^{14}$  W/cm<sup>2</sup>. The black solid lines indicate the negative vector potential  $-\mathbf{A}(t)$  of the laser pulse.

corotating orbitals ( $4p_+^{\uparrow}$  and  $4p_+^{\downarrow}$ ) are larger than those for counter-rotating ones ( $4p_-^{\uparrow}$  and  $4p_-^{\downarrow}$ ), which is due to the initial momentum offset difference between them [38,39]. Here, we are more interested in the comparison between the spin-up and spin-down cases. We can see that the PMD patterns for the  $4p_+^{\uparrow}$  and  $4p_+^{\downarrow}$  (or  $4p_-^{\uparrow}$  and  $4p_-^{\downarrow}$ ) orbitals seem similar to each other, while the corresponding yields are different (see the color scales in Fig. 8).

To further check the SOC effect on the PMDs, we calculate the PEDs and PADs for the  $4p_m^{\uparrow}$  and  $4p_m^{\downarrow}$  orbitals from the corresponding PMDs. The results are illustrated in Fig. 9. From the PEDs shown in Fig. 9(a), one can see that the photoelectrons from the  $4p_+^{\uparrow}$  and  $4p_+^{\downarrow}$  orbitals are generally distributed at a higher kinetic energy than those from the  $4p_-^{\uparrow}$

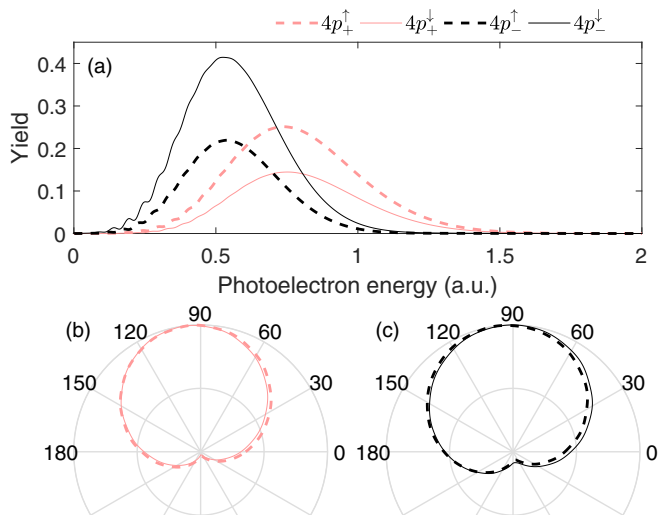


FIG. 9. The (a) PEDs and (b), (c) PADs for the corresponding PMDs in Fig. 8.

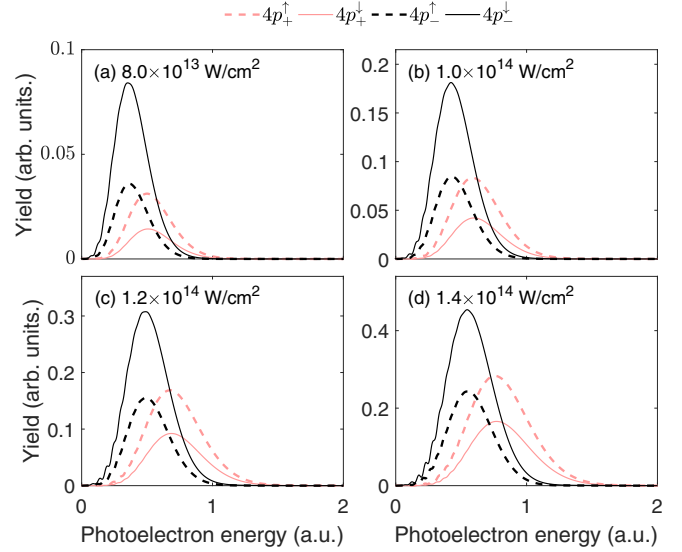


FIG. 10. The PEDs for the  $4p_m^{\uparrow}$  and  $4p_m^{\downarrow}$  orbitals of Kr atom in a three-cycle RCP laser pulse with the wavelength of 800 nm and the intensity of (a)  $I = 8 \times 10^{13}$  W/cm<sup>2</sup>, (b)  $1 \times 10^{14}$  W/cm<sup>2</sup>, (c)  $1.2 \times 10^{14}$  W/cm<sup>2</sup>, and (d)  $1.4 \times 10^{14}$  W/cm<sup>2</sup>, respectively.

and  $4p_-^{\downarrow}$  orbitals. It also shows that the ionization yields are quite different between opposite-spin cases of the same initial angular momentum. Specifically, the ionization yields for the  $4p_+^{\uparrow}$  and  $4p_-^{\downarrow}$  orbitals are, respectively, higher than those for  $4p_+^{\downarrow}$  and  $4p_-^{\uparrow}$ . This is expected, as the  $4p_+^{\uparrow}$  and  $4p_-^{\downarrow}$  orbitals correspond to  $I_p^{3/2}$ , the higher binding energy level where the electron tends to escape more easily. Furthermore, one can find in Fig. 9(a) that the ionization yield for the corotating  $4p_+^{\uparrow}$  orbital is higher than that for the counter-rotating  $4p_-^{\downarrow}$  orbital (dashed curves), whereas it would be the opposite outcome for spinless electrons due to the nonadiabatic effect [40–42]. It indicates that, in this particular case, the SOC effect plays a more significant role over the nonadiabatic effect on the tunneling electron.

Next, we compare the PADs of the  $4p_+$  and  $4p_-$  orbitals with opposite spins, as shown in Figs. 9(b) and 9(c). It can be observed that the SOC effect modifies the PADs to a certain extent for both corotating and counter-rotating orbitals. There could be two aspects that lead to the different PADs for spin-up and spin-down electrons. One is the spin-orbit interaction that deflects the emitting angle of the photoelectron, like the situation of single-photon ionization shown in Figs. 3(g) and 3(h). The other is that the tunnel exits for the spin-up and spin-down electrons of a given  $p_m$  orbital are different, due to the energy-level splitting. The subsequent motions of the spin-up and spin-down electrons after tunneling are therefore deflected differently by the Coulomb potential.

To further discuss the interplay of the SOC effect and the nonadiabatic effect, we illustrate the PEDs for the  $4p_m^{\uparrow}$  and  $4p_m^{\downarrow}$  orbitals at different pulse intensities in Fig. 10. It can be seen that the ionization ratios between counter-rotating and corotating orbitals differ as the pulse intensity changes. Here, we particularly look into the dependence of the PEDs for the  $4p_+^{\uparrow}$  and  $4p_-^{\downarrow}$  orbitals on the pulse intensity, as shown by the dashed curves in Fig. 10. When the pulse intensity is



low enough, the nonadiabatic effect is much more significant and dominates over the SOC effect. In this case, the ionization yield of the counter-rotating  $4p_{-}^{\uparrow}$  orbital is higher than that of the corotating  $4p_{+}^{\uparrow}$  orbital, as shown in Figs. 10(a) and 10(b). This is qualitatively consistent with the prediction of the nonadiabatic tunneling theory [40–42]. As the pulse intensity increases, however, the nonadiabatic effect becomes less significant and the SOC effect plays the main role. The deeper binding energy of the counter-rotating  $4p_{-}^{\uparrow}$  orbital (attributed to the SOC effect) indicates a thicker tunneling barrier, leading to the relatively lower tunneling ionization yield with respect to that of the corotating  $4p_{+}^{\uparrow}$  orbital. In this case, the corotating  $4p_{+}^{\uparrow}$  orbital rather has a higher ionization yield, as shown in Figs. 10(c) and 10(d).

To sum up, in rescattering-free tunneling ionization the SOC effect has impact on the ionization rate and slightly modifies the kinetic and angular distributions of the photoelectrons. Moreover, we show that the competition between the nonadiabatic and SOC effect affects and possibly flips the ionization ratio between the corotating and counter-rotating orbitals driven by circularly polarized pulses.

## V. SUMMARY AND OUTLOOK

In summary, via numerically solving the simplified second-TDPE, we theoretically investigate the effect of spin-orbit coupling in laser-induced ionization of atoms. Our simulations have shown the following: (i) The  $p$  orbitals are no longer degenerate when the electron spin is involved, and the values of the stationary wave functions of  $p$  orbitals are complex numbers instead of pure real numbers in the imaginary-time propagation of the second-TDPE. (ii) In single-photon ionization, the SOC effect not only leads to the electronic kinetic-energy shift, but also deflects the momentum direction of the photoelectron. (iii) In multiphoton ionization, we found a significant difference between the momentum distributions of the spin-up and spin-down photoelectrons. Besides, our numerical results confirm the anomalous emission mode of the photoelectrons from Kr as well as the counterintuitive intensity dependence of the above-threshold ionization spectra, which was reported in the previous experimental studies [9,25]. (iv) In tunneling ionization, the ionization yields are significantly affected due to the spin-orbit energy-level splitting, while the kinetic and angular distributions of the photoelectrons are slightly modified by the SOC effect.

The present work has shown the SOC effect on three selected ionization processes of Kr. By applying the simplified second-TDPE, one will be able to explore in the future the SOC effect on more strong-field phenomena following laser-driven ionization of noble gas atoms. On the other hand, we will work on the numerical solution in three-dimensional space for the coupled equations of Eqs. (3) and (4) that include the spin-flip process, as controlling the spin flip with lasers is also an interesting topic to the strong-field community.

## ACKNOWLEDGMENTS

K.L. and K.R. gratefully thank Ingo Barth for years of support and fruitful discussion and collaboration. This work is supported by National Natural Science Foundation of China

(Grants No. 12174133, No. 11874163, and No. 12021004) and the Innovation Project of Optics Valley Laboratory (Grant No. OVL2021ZD001). The computing work in this paper is supported by the Public Service Platform of High Performance Computing by Network and Computing Center of HUST.

## APPENDIX: JUSTIFICATIONS OF THE APPROXIMATIONS

In our modeling, we omit several relativistic corrections in the second-TDPE, including the nondipole effect, the Zeeman term, the relativistic correction of the kinetic energy, and the Darwin term. In this Appendix, we present the justifications of these approximations.

### 1. The nondipole effect

In the present work, the nondipole effect is manifested in two aspects. One is the nondipole effect on the SOC. Considering the spatial dependence of the laser pulse, the spin-orbit interaction term in the second-TDPE is given by

$$\begin{aligned}\hat{H}_{\text{so}} &= \frac{1}{8c^2} [\hat{\mathbf{P}}(\boldsymbol{\sigma} \times \mathbf{E}) + (\boldsymbol{\sigma} \times \mathbf{E})\hat{\mathbf{P}}] \\ &= \frac{1}{4c^2} \boldsymbol{\sigma}(\mathbf{E} \times \hat{\mathbf{P}}) - \frac{i}{8c^2} \boldsymbol{\sigma}(\nabla \times \mathbf{E}),\end{aligned}\quad (\text{A1})$$

where the electric field is defined as  $\mathbf{E} = -\nabla V - \partial \mathbf{A} / \partial t$ . Since  $\nabla \times (\nabla V) = \mathbf{0}$  for the central potential  $V = V(r)$ , we have

$$\nabla \times \mathbf{E} = -\nabla \times \left( \nabla V + \frac{\partial \mathbf{A}}{\partial t} \right) = -\frac{\partial}{\partial t} (\nabla \times \mathbf{A}) = O\left(\frac{1}{c}\right).\quad (\text{A2})$$

Thus, the nondipole effect on the SOC is of third order in  $1/c$ , and it can be neglected safely.

The other aspect of the nondipole effect is its influence on the electronic dynamics in the  $\hat{\mathbf{P}}^2/2$  term in the second-TDPE. For a laser pulse polarized in the  $x$ - $y$  plane and propagating in the  $\mathbf{e}_z$  direction, the vector potential of the laser pulse can be represented as  $\mathbf{A}(\eta) = A_x(\eta)\mathbf{e}_x + A_y(\eta)\mathbf{e}_y = (A_x(\eta), A_y(\eta))$ , where  $\eta = t - z/c$  is the light cone time. Thus, the corresponding electric fields and magnetic fields are  $\mathbf{E}(\eta) = -\partial \mathbf{A}(\eta) / \partial t = (E_x(\eta), E_y(\eta))$  and  $\mathbf{B}(\eta) = \nabla \times \mathbf{A}(\eta) = (B_x(\eta), B_y(\eta))$ . In the nonrelativistic limit, the Lorentz equation for an electron in this laser pulse is

$$\frac{d}{dt} \mathbf{v} = -[\mathbf{E}(\eta) + \mathbf{v} \times \mathbf{B}(\eta)],\quad (\text{A3})$$

where  $\mathbf{v}$  is the electron velocity. Including terms of the order of  $1/c$  in Eq. (A3), the electronic dynamics is governed by

$$\begin{aligned}\frac{d}{dt} v_x &= -E_x(t), \\ \frac{d}{dt} v_y &= -E_y(t), \\ \frac{d}{dt} v_z &= v_x B_y(t) - v_y B_x(t).\end{aligned}\quad (\text{A4})$$

One can see that the nondipole effect on the  $\hat{\mathbf{P}}^2/2$  term slightly alters the momentum shift of the photoelectron in the

direction of laser propagation, whereas it hardly changes the electron motion in the plane of polarization of the laser pulse. This has been confirmed in the previous studies [43–45]. Moreover, the nondipole effect has the same impact on the electrons carrying opposite spins and thus it will not affect our investigation of the SOC effect. Finally, in experiments, if it is desired, the nondipole effect can be suppressed by applying two counterpropagating pulses [46].

Therefore, as long as we are focusing on the SOC effect on the electronic dynamics in the plane of polarization of the laser pulse, we can safely omit the nondipole effect for the studies.

## 2. The Zeeman term $\sigma\mathbf{B}/(2c)$

Supposing the laser pulse is propagated along the  $\mathbf{e}_z$  direction, we have  $\mathbf{B} = \nabla \times \mathbf{A}(z, t) = (B_x, B_y)$ . Thus, the Zeeman term can be written as

$$\begin{aligned} \frac{1}{2c}\sigma\mathbf{B} &= \frac{1}{2c}(\sigma_x B_x + \sigma_y B_y) \\ &= \frac{1}{2c} \begin{pmatrix} 0 & B_x + iB_y \\ B_x - iB_y & 0 \end{pmatrix}. \end{aligned} \quad (\text{A5})$$

Considering its effect on the two-spinor  $\Psi = (\psi^\uparrow, \psi^\downarrow)^T$ , we get

$$\begin{aligned} i\frac{\partial}{\partial t} \begin{pmatrix} \psi^\uparrow \\ \psi^\downarrow \end{pmatrix} &= \frac{1}{2c}\sigma\mathbf{B} \begin{pmatrix} \psi^\uparrow \\ \psi^\downarrow \end{pmatrix} \\ &= \frac{1}{2c} \begin{pmatrix} 0 & B_x + iB_y \\ B_x - iB_y & 0 \end{pmatrix} \begin{pmatrix} \psi^\uparrow \\ \psi^\downarrow \end{pmatrix}. \end{aligned} \quad (\text{A6})$$

Then, we obtain the coupled equations for the wave functions of the spin-up and spin-down electrons as

$$i\frac{\partial\psi^\uparrow}{\partial t} = \frac{1}{2c}(B_x + iB_y)\psi^\downarrow, \quad (\text{A7})$$

$$i\frac{\partial\psi^\downarrow}{\partial t} = \frac{1}{2c}(B_x - iB_y)\psi^\uparrow. \quad (\text{A8})$$

It is clear that the Zeeman term contributes to the spin-flip process, which can be safely omitted once the pulse intensity is in the nonrelativistic regime (related discussions can be found in the Ref. [11]).

## 3. The relativistic correction of the kinetic-energy term $-\hat{\Pi}^4/(8c^2)$

The ratio between this relativistic correction to the nonrelativistic kinetic energy is

$$\frac{V_e^4/(8c^2)}{V_e^2/c} = \frac{V_e^2}{4c^2}, \quad (\text{A9})$$

where  $V_e$  represents the speed of the electron. For the ionization scenarios considered in the current research, we have  $V_e \leq 2$  a.u.  $< c \times 1.5\%$ , and thus  $V_e^2/(4c^2) < 5.625 \times 10^{-5}$ . So, the speed of the electron is sufficiently below the relativistic limit and this relativistic correction can be neglected.

## 4. The Darwin term $\nabla\mathbf{E}/(8c^2)$

From the definition of the electric field  $\mathbf{E}(\mathbf{r}, t)$ , it can be split into two terms: (i) The atomic term  $\mathbf{E}_A(r) = -\nabla V(r)$ , with  $V(r)$  defined by Eq. (6). (ii) The laser field term  $\mathbf{E}_L(z, t) = -\partial\mathbf{A}(z, t)/\partial t$ . Then, the divergences of the electric field in the Darwin term can be written as

$$\nabla\mathbf{E}(\mathbf{r}, t) = \nabla\mathbf{E}_A(r) + \nabla\mathbf{E}_L(z, t). \quad (\text{A10})$$

For  $\nabla\mathbf{E}_L(z, t)$ , we get

$$\nabla\mathbf{E}_L(z, t) = \frac{\partial}{\partial x}E_{L,x}(z, t) + \frac{\partial}{\partial y}E_{L,y}(z, t) = 0, \quad (\text{A11})$$

since  $E_{L,x}(z, t)$  and  $E_{L,y}(z, t)$  do not depend on the coordinates  $x$  and  $y$ . For  $\nabla\mathbf{E}_A(r)$ , we regard that

$$\mathbf{E}_A(r) = -\frac{\partial V(r)}{\partial r}\mathbf{e}_r, \quad (\text{A12})$$

and one can easily find that  $\nabla\mathbf{E}_A$  is a function of  $r$ . From the numerical point of view, such correction plays a similar role as the potential parameters to adjust the ionization potentials. Eventually, the Darwin term  $\nabla\mathbf{E}/(8c^2) = (\nabla\mathbf{E}_A + \nabla\mathbf{E}_L)/(8c^2)$  can be interpreted as a small relativistic correction to the Coulomb potential  $V(r)$ . On the other hand, the Darwin term correction is identical for both spin-up and spin-down electrons. Therefore, omitting the Darwin term will not affect our investigation of the spin-orbit interaction.

- 
- [1] G. E. Uhlenbeck and S. Goudsmit, Spinning electrons and the structure of spectra, *Nature (London)* **117**, 264 (1926).
- [2] M. S. Altman, H. Pinkvos, J. Hurst, H. Poppa, G. Marx, and E. Bauer, Spin polarized low energy electron microscopy of surface magnetic structure, *Mater. Res. Soc. Symp. Proc.* **232**, 125 (1991).
- [3] Q. Wu, R. Zdyb, E. Bauer, and M. S. Altman, Growth, magnetism and ferromagnetic thickness gap in Fe films on the W(111) surface, *Phys. Rev. B* **87**, 104410 (2013).
- [4] H. F. Ding, A. K. Schmid, D. Li, K. Y. Guslienko, and S. D. Bader, Magnetic Bistability of Co Nanodots, *Phys. Rev. Lett.* **94**, 157202 (2005).
- [5] I. Barth and O. Smirnova, Spin-polarized electrons produced by strong-field ionization, *Phys. Rev. A* **88**, 013401 (2013).
- [6] A. Hartung, F. Morales, M. Kunitski, K. Henrichs, A. Laucke, M. Richter, T. Jahnke, A. Kalinin, M. Schöffler, L. Ph. H. Schmidt, M. Ivanov, O. Smirnova, and R. Dörner, Electron spin polarization in strong-field ionization of xenon atoms, *Nat. Photonics* **10**, 526 (2016).
- [7] M.-M. Liu, Y. Shao, M. Han, P. Ge, Y. Deng, C. Wu, Q. Gong, and Y. Liu, Energy- and Momentum-Resolved Photoelectron Spin Polarization in Multiphoton Ionization of Xe by Circularly Polarized Fields, *Phys. Rev. Lett.* **120**, 043201 (2018).
- [8] D. Trabert, A. Hartung, S. Eckart, F. Trinter, A. Kalinin, M. Schöffler, L. Ph. H. Schmidt, T. Jahnke, M. Kunitski, and R. Dörner, Spin and Angular Momentum in Strong-Field Ionization, *Phys. Rev. Lett.* **120**, 043202 (2018).
- [9] M. Han, P. Ge, Y. Fang, X. Yu, Z. Guo, Y. Deng, C. Wu, Q. Gong, and Y. Liu, Doubly excited electron-ion angular

- momentum transfer in parity-unfavored multiphoton ionization, *Phys. Rev. A* **101**, 061401(R) (2020).
- [10] I. A. Ivanov, Relativistic calculation of the electron-momentum shift in tunneling ionization, *Phys. Rev. A* **91**, 043410 (2015).
- [11] I. A. Ivanov, Spin-flip processes and nondipole effects in above-threshold ionization of hydrogen in ultrastrong laser fields, *Phys. Rev. A* **96**, 013419 (2017).
- [12] T. Kjellsson, S. Selstø, and E. Lindroth, Relativistic ionization dynamics for a hydrogen atom exposed to superintense XUV laser pulses, *Phys. Rev. A* **95**, 043403 (2017).
- [13] D. A. Tumakov, D. A. Telnov, G. Plunien, V. A. Zaytsev, and V. M. Shabaev, Relativistic mask method for electron momentum distributions after ionization of hydrogen-like ions in strong laser fields, *Eur. Phys. J. D* **74**, 188 (2020).
- [14] J. Wragg, C. Ballance, and H. van der Hart, Breit-Pauli  $r$ -matrix approach for the time-dependent investigation of ultrafast processes, *Comput. Phys. Commun.* **254**, 107274 (2020).
- [15] K. Renziehausen, K. Liu, and I. Barth, How to approximate the Dirac equation with the Mauser method, *Quantum Stud.: Math. Found.* **9**, 287 (2022).
- [16] M. D. Feit, J. A. Fleck, Jr., and A. Steiger, Solution of the Schrödinger equation by a spectral method, *J. Comput. Phys.* **47**, 412 (1982).
- [17] J. Douglas Jr., Alternating direction methods for three space variables, *Numer. Math.* **4**, 41 (1962).
- [18] J. Crank and P. Nicolson, A practical method for numerical evaluation of solutions of partial differential equations of the heat-conduction type, *Math. Proc. Cambridge Philos. Soc.* **43**, 50 (1947).
- [19] S. Chelkowski, C. Foisy, and A. D. Bandrauk, Electron-nuclear dynamics of multiphoton  $H_2^+$  dissociative ionization in intense laser fields, *Phys. Rev. A* **57**, 1176 (1998).
- [20] X. M. Tong, K. Hino, and N. Toshima, Phase-dependent atomic ionization in few-cycle intense laser fields, *Phys. Rev. A* **74**, 031405(R) (2006).
- [21] Y. Fu, J. Zeng, and J. Yuan, PCTDSE: A parallel Cartesian-grid-based TDSE solver for modeling laser-atom interactions, *Comput. Phys. Commun.* **210**, 181 (2017).
- [22] M. Protopapas, C. H. Keitel, and P. L. Knight, Atomic physics with super-high intensity lasers, *Rep. Prog. Phys.* **60**, 389 (1997).
- [23] B. P. Acharya, M. Dodson, S. Dubey, K. L. Romans, A. H. N. C. De Silva, K. Foster, O. Russ, K. Bartschat, N. Douguet, and D. Fischer, Magnetic dichroism in few-photon ionization of polarized atoms, *Phys. Rev. A* **104**, 053103 (2021).
- [24] X. Xie, A. Scrinzi, M. Wickenhauser, A. Baltuška, I. Barth, M. Kitzler, Internal Momentum State Mapping Using High Harmonic Radiation, *Phys. Rev. Lett.* **101**, 033901 (2008).
- [25] M. Nakano, T. Otobe, and R. Itakura, Anomalous photoelectron angular distribution in ionization of Kr in intense ultraviolet laser fields, *Phys. Rev. A* **95**, 063404 (2017).
- [26] H. G. Muller, G. Petite, and P. Agostini, Comment on "Asymmetries in Above-Threshold Ionization," *Phys. Rev. Lett.* **61**, 2507 (1988).
- [27] G. Petite, P. Agostini, and H. G. Muller, Intensity dependence of non-perturbative above-threshold ionization spectra: Experimental study, *J. Phys. B: At., Mol. Opt. Phys.* **21**, 4097 (1988).
- [28] W. Becker, F. Grasbon, R. Kopold, D. B. Milošević, G. G. Paulus, and H. Walther, Above-threshold ionization: From classical features to quantum effects, *Adv. At. Mol. Opt. Phys.* **48**, 35 (2002).
- [29] F. Krausz and M. Ivanov, Attosecond physics, *Rev. Mod. Phys.* **81**, 163 (2009).
- [30] W. Becker, X. Liu, P. J. Ho, and J. H. Eberly, Theories of photoelectron correlation in laser-driven multiple atomic ionization, *Rev. Mod. Phys.* **84**, 1011 (2012).
- [31] L. Y. Peng, W. C. Jiang, J. W. Geng, W. H. Xiong, and Q. H. Gong, Tracing and controlling electronic dynamics in atoms and molecules by attosecond pulses, *Phys. Rep.* **575**, 1 (2015).
- [32] J. Liang, Y. Zhou, Y. Liao, W.-C. Jiang, M. Li, and P. Lu, Direct visualization of deforming atomic wavefunction in ultraintense high-frequency laser pulses, *Ultrafast Sci.* **2022**, 9842716 (2022).
- [33] P. Eckle, A. N. Pfeiffer, C. Cirelli, A. Staudte, R. Dörner, H. G. Muller, M. Büttiker, and U. Keller, Attosecond ionization and tunneling delay time measurements in helium, *Science* **322**, 1525 (2008).
- [34] A. S. Landsman, M. Weger, J. Maurer, R. Boge, A. Ludwig, S. Heuser, C. Cirelli, L. Gallmann, and U. Keller, Ultrafast resolution of tunneling delay time, *Optica* **1**, 343 (2014).
- [35] U. Sainadh, H. Xu, X. Wang, A. Atia-Tul-Noor, W. Wallace, N. Douguet, A. Bray, I. Ivanov, K. Bartschat, A. Kheifets, R. Sang, and I. Litvinyuk, Attosecond angular streaking and tunnelling time in atomic hydrogen, *Nature (London)* **568**, 75 (2019).
- [36] A. N. Pfeiffer, C. Cirelli, M. Smolarski, D. Dimitrovski, M. Abu-samaha, L. B. Madsen, and U. Keller, Attoclock reveals natural coordinates of the laser-induced tunnelling current flow in atoms, *Nat. Phys.* **8**, 76 (2012).
- [37] K. Liu, S. Luo, M. Li, Y. Li, Y. Feng, B. Du, Y. Zhou, P. Lu, and I. Barth, Detecting and Characterizing the Nonadiabaticity of Laser-Induced Quantum Tunneling, *Phys. Rev. Lett.* **122**, 053202 (2019).
- [38] I. Barth and O. Smirnova, Nonadiabatic tunneling in circularly polarized laser field. II. Derivation of formulas, *Phys. Rev. A* **87**, 013433 (2013).
- [39] J. Kaushal, F. Morales, and O. Smirnova, Opportunities for detecting ring currents using an attoclock setup, *Phys. Rev. A* **92**, 063405 (2015).
- [40] I. Barth and O. Smirnova, Nonadiabatic tunneling in circularly polarized laser fields: Physical picture and calculations, *Phys. Rev. A* **84**, 063415 (2011).
- [41] T. Herath, L. Yan, S. K. Lee, and W. Li, Strong-Field Ionization Rate Depends on the Sign of the Magnetic Quantum Number, *Phys. Rev. Lett.* **109**, 043004 (2012).
- [42] S. Eckart, M. Kunitski, M. Richter, A. Hartung, J. Rist, F. Trinter, K. Fehre, N. Schlott, K. Henrichs, L. P. H. Schmidt, T. Jahnke, M. Schöffler, K. Liu, I. Barth, J. Kaushal, F. Morales, M. Ivanov, O. Smirnova, and R. Dörner, Ultrafast preparation and detection of ring currents in single atoms, *Nat. Phys.* **14**, 701 (2018).
- [43] S. Brennecke and M. Lein, High-order above-threshold ionization beyond the electric dipole approximation: Dependence on the atomic and molecular structure, *Phys. Rev. A* **98**, 063414 (2018).
- [44] S. Brennecke and M. Lein, High-order above-threshold ionization beyond the electric dipole approximation, *J. Phys. B: At., Mol. Opt. Phys.* **51**, 094005 (2018).

- [45] H. Ni, S. Brennecke, X. Gao, P.-L. He, S. Donsa, I. Březinová, F. He, J. Wu, M. Lein, X.-M. Tong, and J. Burgdörfer, Theory of Subcycle Linear Momentum Transfer in Strong-Field Tunneling Ionization, *Phys. Rev. Lett.* **125**, 073202 (2020).
- [46] A. Hartung, S. Eckart, S. Brennecke, J. Rist, D. Trabert, K. Fehre, M. Richter, H. Sann, S. Zeller, K. Henrichs, G. Kastirke, J. Hoehl, A. Kalinin, M. S. Schöffler, T. Jahnke, L. Ph. H. Schmidt, M. Lein, M. Kunitski, and R. Dörner, Magnetic fields alter strong-field ionization, *Nat. Phys.* **15**, 1222 (2019).